



Infrared Spectra, Optical Constants, and Temperature Dependences of Amorphous and Crystalline Benzene Ices Relevant to Titan

Delphine Nna-Mvondo^{1,2}  and Carrie M. Anderson²¹ University of Maryland Baltimore County (UMBC), Center for Space Sciences and Technology (CSST), 1000 Hilltop Circle, Baltimore, MD 21250, USA
dnnamvo@umbc.edu, dnnamvondo@gmail.com² NASA Goddard Space Flight Center, 8800 Greenbelt Road, Greenbelt, MD 20771, USA

Received 2020 January 14; revised 2021 October 18; accepted 2021 October 29; published 2022 February 1

Abstract

Benzene ice contributes to an emission feature detected by the Cassini Composite InfraRed Spectrometer (CIRS) near 682 cm^{-1} in Titan's late southern fall polar stratosphere. It is also one of the dominant components of the CIRS-observed High-Altitude South Polar ice cloud observed in Titan's mid stratosphere during late southern fall. Titan's stratosphere exhibits significant seasonal changes with temperatures that spatially vary with seasons. A quantitative analysis of the chemical composition of infrared emission spectra of Titan's stratospheric ice clouds relies on consistent and detailed laboratory transmittance spectra obtained at numerous temperatures. However, there is a substantial lack of experimental data on the spectroscopic and optical properties of benzene ice and its temperature dependence, especially at Titan-relevant stratospheric conditions. We have therefore analyzed in laboratory the spectral characteristics and evolution of benzene ice's vibrational modes at deposition temperatures ranging from 15 to 130 K, from the far- to mid-IR spectral region ($50\text{--}8000\text{ cm}^{-1}$). We have determined the amorphous-to-crystalline phase transition of benzene ice and identified that a complete crystallization is achieved for deposition temperatures between 120 and 130 K. We have also measured the real and imaginary parts of the ice complex refractive index of benzene ice from 15 to 130 K. Our experimental results significantly extend the current state of knowledge on the deposition temperature dependence of benzene ice over a broad infrared spectral range, and provide useful new data for the analysis and interpretation of Titan-observed spectra.

Unified Astronomy Thesaurus concepts: Saturnian satellites (1427); Titan (2186); Ice formation (2092); Molecular spectroscopy (2095); Transmission spectroscopy (2133); Astrochemistry (75); Planetary atmospheres (1244); Laboratory astrophysics (2004); Far infrared astronomy (529); Near infrared astronomy (1093); Experimental techniques (2078)

1. Introduction

Benzene (C_6H_6), the simplest aromatic hydrocarbon, is a molecule that has raised great interest in the astrophysical community for almost four decades. This is mainly because C_6H_6 is one of the main precursors of polycyclic aromatic hydrocarbons (PAHs) reported to be present in interstellar dust particles (Leger & Puget 1984; Allamandola et al. 1989; Tielens 2013 and references therein), carbonaceous chondrites (Pering & Ponnampertuma 1971; Hayatsu et al. 1977; Hahn et al. 1988), and other astrophysical environments, such as carbon-rich, high-temperature environments (circumstellar and carbon-rich protoplanetary nebulae; Buss et al. 1993; Clemett et al. 1994). Benzene rings easily produce more complex, polycyclic structures by the one-ring build-up mechanism (Simoneit & Fetzer 1996). In space, an analogous process to carbon soot formation occurring on Earth can be initiated through the completion of that first aromatic ring and may also lead to the synthesis of PAHs (Tielens & Charnley 1997). Mechanisms involving the addition of hydrocarbons, such as acetylene onto aromatic rings as well as the attachment of other aromatic rings, or hydrocarbon pyrolysis, have been proposed to characterize the growth process of PAHs (Bittner & Howard 1981; Frenklach & Feigelson 1989; Wang & Frenklach 1997; Cherchneff 2011 and references therein).

PAH synthesis from shocked benzene has also been reported (Mimura 1995). PAHs are crucial materials involved in a variety of cosmochemical processes. For example, amino acids could be synthesized by aqueous alteration of precursor PAHs in carbonaceous chondrites (Shock & Schulte 1990). PAHs are also produced in laboratory-simulated planetary atmospheres of Titan and Jupiter (Sagan et al. 1993; Khare et al. 2002; Trainer et al. 2004), and results from these studies indicate that the formation of aromatic rings and polyaromatics may be, among other sources, a possible chemical pathway for the production of the atmospheric solid particles (Lebonnois et al. 2002; Wilson et al. 2003; Trainer et al. 2004). The formation and evolution of benzene in planetary environments or other solar system objects thus represents a fundamental primary stage of the PAH production and other subsequent relevant chemical and prebiotic processes (like soot formation). In this context, several works related to benzene have been devoted to better understand the physico-chemical processes of irradiated C_6H_6 , in its gaseous and solid phases, and the derived products, by acquiring high-resolution astronomical spectra, carrying out detailed laboratory studies or developing theoretical modeling (Allamandola et al. 1989 and references therein; Callahan et al. 2013; Materese et al. 2015; Mouzay et al. 2021). Laboratory astrophysical investigations have mostly focused on performing vibrational spectroscopy of ion, electron, or UV irradiated C_6H_6 gas and C_6H_6 ice. Such investigations aim to provide data on the spectral properties of the irradiated C_6H_6 materials, compare them with spectra obtained from astronomical observations (e.g., observations of the interstellar medium),



Original content from this work may be used under the terms of the [Creative Commons Attribution 4.0 licence](https://creativecommons.org/licenses/by/4.0/). Any further distribution of this work must maintain attribution to the author(s) and the title of the work, journal citation and DOI.

or to study photoprocessed benzene ices to understand the fate of benzene ices in Titan's stratosphere and help understanding the formation of aerosol analogs observed in Saturn's moon's stratosphere (Mouzay et al. 2021).

Our experimental study differs from such previous works. The main objective was to carry out a comprehensive experimental study on pristine benzene ice in order to accurately determine its chemical behavior and its infrared (IR) and optical properties at different deposition temperatures. The initial motivation behind our laboratory experiments was to constrain the role of benzene in the formation and chemical composition of Titan's High-Altitude South Polar (HASP) ice cloud. The HASP ice cloud is a massive stratospheric ice cloud system, recently observed in far-IR limb spectra recorded by the Cassini Composite InfraRed Spectrometer (CIRS) in Titan's late southern fall mid stratosphere (~ 200 km altitude), at high southern polar latitudes (Anderson et al. 2018b).

During the Cassini mission, one of the highly unexpected findings was the detection of benzene gas in Titan's upper atmosphere, as determined by in situ analyses by the Cassini Plasma Spectrometer (CAPS) and the Ion Neutral Mass Spectrometer (INMS) performed during Cassini's first close flybys of Titan (Coates et al. 2007; Waite et al. 2007). During subsequent Titan flybys, C_6H_6 gas was also observed by Cassini CIRS in Titan's stratosphere, at high northern and high southern latitudes (Coustenis et al. 2013, 2016, 2018). Atmospheric C_6H_6 gas, produced through the photodissociation of gaseous N_2-CH_4 in Titan's upper atmosphere and successive ion-neutral reactions (Vuitton et al. 2008), enters altitude regions in Titan's stratosphere where it can saturate and condense. Vinatier et al. (2018) reported the contribution of the ν_4 vibrational mode of benzene ice with other unidentified molecules during the observation of Titan's south polar stratospheric cloud at mid-to-upper-stratospheric altitudes during southern fall, using CIRS nadir and limb observations in 2013 May and 2015 March, respectively. Anderson et al. (2018b) reported that later, in 2015 July during Titan's late southern fall, C_6H_6 condenses at altitudes where the HASP cloud vertically resides (Figure 1), deeper in the stratosphere than the C_6H_6 ice cloud reported by Vinatier et al. (2018). The Anderson et al. (2018b) investigators experimentally demonstrated that C_6H_6 co-condensed with other organic ice components, likely contributes to the chemical composition of Titan's HASP ice cloud. The temperatures in Titan's mid-to-low stratosphere range from ~ 66 to 170 K (Schinder et al. 2011; Anderson et al. 2014; Teanby et al. 2019) and experience variations with altitude and season. Given that IR spectral features depend on the thermal excitation of the crystal's vibrational modes, laboratory IR spectra of ices measured at various low and high temperatures, including the thermal conditions at different altitudes in Titan's atmosphere, can considerably improve the accuracy of the interpretation of IR emission spectra obtained from remote sensing observations. Particularly, studying the deposition temperature dependences of benzene ice is necessary to constrain its spectral and optical properties, and ultimately its contribution to Titan's cloudy stratosphere during winter seasons, because the temperature may alter the peak positions, widths, and shapes of the absorption bands of C_6H_6 ice.

However, no such thorough study has been performed and reported for benzene ice related to Titan studies. The literature reports few works on the temperature effects on solid benzene (Mair & Hornig 1949; Hollenberg & Dows 1962; Ishii et al. 1996; Mouzay et al. 2021). However, the studies of

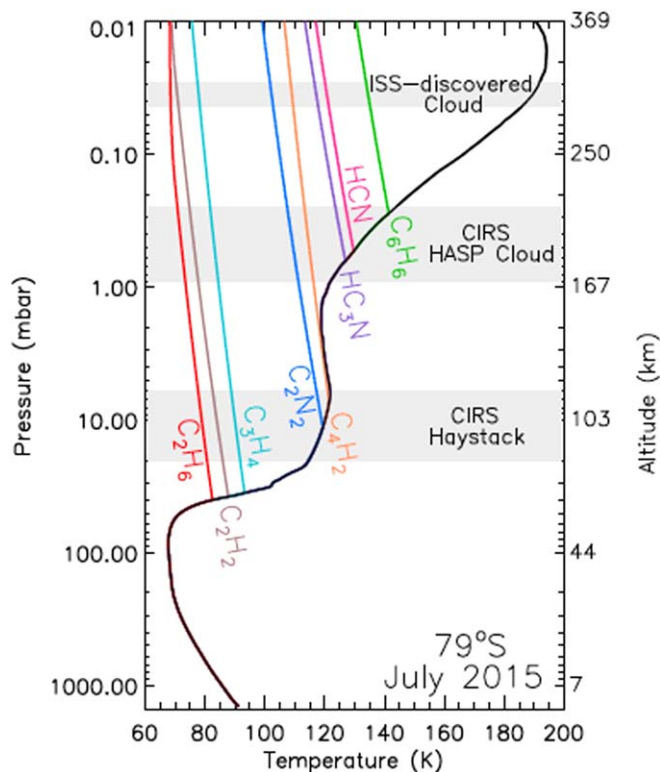


Figure 1. Figure 1 from Anderson et al. (2018b). Titan's pressure-temperature-altitude profile (black curve) at $79^\circ S$ during late southern fall (2015 July) and vertical distributions for eight of Titan's stratospheric organic vapors (color-coded curves). The intersection between temperature profile and the saturation vapor pressure curves provides the estimated altitude location for the condensation of each individual vapor. The saturation vapor pressure for benzene was taken from Fray & Schmitt (2009).

Mair & Hornig (1949), Hollenberg & Dows (1962), and Ishii et al. (1996) focused on solid C_6H_6 at specific temperatures and did not span a wide range of temperatures that extend from the amorphous to crystalline phases. For example, Mair & Hornig (1949) recorded IR spectra of C_6H_6 ice obtained from the crystallization of the C_6H_6 liquid phase at 249, 218, and 103 K from 641 to 5000 cm^{-1} ($15.6\text{--}2\text{ }\mu\text{m}$), and Hollenberg & Dows (1962) from condensed C_6H_6 gas at 85 K and annealed crystalline C_6H_6 ice at 155 K from 550 to 1600 cm^{-1} ($18.2\text{--}6.25\text{ }\mu\text{m}$). Ishii et al. (1996) focused on Raman spectroscopy of C_6H_6 ice deposited from 17 to 78 K and the annealed ice from 17 to 98 K, while the work of Mouzay et al. (2021) reported annealed 16 K- C_6H_6 ice from 70 to 130 K and not C_6H_6 ice directly deposited at different temperatures, which is more appropriate to Titan's ice cloud studies, as explained later in Section 2.

In this work, we have conducted a systematic and thorough study of benzene ice with the vapors directly deposited at several temperatures between 15 and 150 K. Deposition temperatures between 66 and 130 K are comparable to the condensation temperatures in Titan's mid-to-low stratosphere. We decided to extend the spectral analysis to deposition temperatures lower than 66 K in order to fully understand the behavior of C_6H_6 ice with temperature changes, and to precisely identify the transition from its amorphous to crystalline phase in our laboratory sample. Direct vapor deposition studies (as opposed to annealing experiments) are almost nonexistent and are crucial to identify the chemical composition of Titan's CIRS-observed stratospheric ice clouds.

2. Experimental Technique

Thin film transmission spectroscopy of amorphous and crystalline phases of pure benzene ice was conducted using the SPECTROscopy of Titan-Related ice AnaLogs (SPECTRAL) ice high-vacuum chamber (Anderson et al. 2018a; Nna-Mvondo et al. 2019), located at NASA Goddard Space Flight Center. The technique, used in our laboratory for the IR spectroscopy of ice analogs, consists of depositing the vapor of one or several molecules onto a cold diamond substrate maintained at low temperature (15–200 K) by a close-cycle helium cryostat. A thin ice film ($\leq 10 \mu\text{m}$) forms on the diamond substrate, and its spectral properties are monitored in real-time and in situ through a Fourier transform infrared (FTIR) spectrometer. A complete description of the SPECTRAL ice chamber, along with the standard experimental methodology for vapor deposition and data analyses utilized in the present work, is detailed in Anderson et al. (2018a).

C_6H_6 ice samples were prepared from pure benzene vapors that were obtained at saturation equilibrium from the purified liquid phase evaporated at room temperature (293 K). At room temperature, benzene has a saturation vapor pressure of 100 mbar. Benzene (Sigma-Aldrich, 99.99% HPLC grade) was purified from air contaminants (predominantly water and carbon dioxide) and other trace organic impurities, by freeze-pump-thaw cycling under vacuum using successive cold baths of ethanol ($\text{C}_2\text{H}_5\text{OH}$)/liquid nitrogen (LN_2) (157 K) and acetone ($\text{C}_2\text{H}_6\text{CO}$)/ LN_2 (179 K). Afterwards, purified C_6H_6 was stored for further use in vacuo in an ultra-low-temperature freezer at -86°C (187 K).

The thin C_6H_6 ice films were obtained by slow deposition of pure benzene gas onto the diamond substrate inside the SPECTRAL chamber, under vacuum (10^{-8} mbar), at a flow rate of $0.66 \text{ ml minute}^{-1}$, at the desired low temperature, with an ice deposition rate of $0.56 \mu\text{m minute}^{-1}$. The distance from the injection nozzles to the diamond substrate is $\sim 1.3 \text{ cm}$. Warming and cooling rates of the diamond substrate on which the ice deposits were $4.8 \text{ K minute}^{-1}$ and $1.3 \text{ K minute}^{-1}$, respectively. The temperature was controlled with an accuracy of $\pm 0.5 \text{ K}$ from 2 to 305 K by a temperature controller connected to the cryocooler, a 36Ω internal resistive Thermofoil heater, and two silicon diodes (accuracy $\pm 0.5 \text{ K}$ from 2 to 305 K). One of the diodes is located on the holder of the diamond substrate, which measures the temperature of the sample, and the other one is on the cold finger of the cryocooler (Anderson et al. 2018a). The thicknesses of the ice films at each deposition temperature (T_d) were determined by double laser interferometry (detailed in Anderson et al. 2018a, Section 4.3) and using the published n_0 value of 1.54 ± 0.02 at 632.8 nm for benzene ice formed after vapor deposition at 100 K determined by Romanescu et al. (2010). The calculated thickness for C_6H_6 ice films ranged between 3.6 and $4.1 \mu\text{m}$, which corresponds to 26 and $30 \mu\text{mol}$ of benzene, respectively.

We decided to obtain the crystalline benzene ice from direct deposition of C_6H_6 vapor at low temperature rather than by annealing³ the sample, a technique commonly used to achieve the crystallization of an ice for most of the planetary ice

laboratory studies found in the literature (e.g., Hollenberg & Dows 1962; Khanna et al. 1988; Kim & Kaiser 2009; Zhou et al. 2009; Mouzay et al. 2021). As we demonstrated with $\text{C}_2\text{H}_5\text{CN}$ ice in a recent study by Nna-Mvondo et al. (2019), the annealing experimental method raises important concerns about the quality of the crystalline phase of the annealed ice. Indeed, in this previous work, we revealed spectral differences between the directly deposited crystalline ice and the annealed ice, indicating that the ice does not reach complete crystallization when annealed, and a portion of the amorphous structure is irreversibly retained in the final crystalline phase. The observed spectral variabilities also affect the optical constants of the ice being studied, i.e., the real (n) and imaginary (k) parts of the ice complex refractive index (or optical constants), which are needed for radiative transfer fits to observed spectra. Additionally, the annealing experimental approach, although appropriate to study ices formed in the interstellar medium, is not applicable for simulating ices formed in planetary atmospheres, such as Titan’s stratosphere. For example, for Titan, in order to reproduce ice cloud formation in the stratosphere, vapors must be directly deposited at warmer temperatures (e.g., 110 K), since most of Titan’s organic vapors condense as the vapors cool while descending throughout Titan’s stratosphere (as seen in Figure 1).

The spectra of C_6H_6 thin ice films were collected at deposition temperatures ranging from 15 to 150 K, in the far-to mid-IR spectral region ($50\text{--}8000 \text{ cm}^{-1}$; $200\text{--}1.25 \mu\text{m}$). For each resulting transmittance spectrum, 256 scans were averaged at a spectral resolution of 4 cm^{-1} . The motivation of our work was to use the experimental spectral data that we collected for studying and interpreting the stratospheric HASP ice cloud observed by CIRS in far-IR limb spectra. The spectral dependences of the majority of the CIRS-observed stratospheric ice clouds were determined from analyses of CIRS far-IR-targeted low-spectral-resolution limb scans acquiring many low-resolution spectra, as it was desirable in some circumstances, like during observations of strong gas emissions such as methane. Specifically, for the HASP ice cloud observations, the type of far-IR limb observation used was the far-IR aerosol scan (FIRLMBAER), the second-closest observation to Titan, occurring at $(15\text{--}25) 10^3 \text{ km}$ ($45\text{--}75$ minutes from closest approach), using a spectral resolution of 15 cm^{-1} (the lowest spectral resolution of CIRS). For this reason, the resolution of 4 cm^{-1} for the collection of our experimental spectra was very convenient and relevant for the objective of our experimental study.

In the mid-IR, the FTIR spectrometer’s gain and aperture size were initially optimized to reduce the intensity of the chemical vapor deposition (CVD) diamond’s strong absorption bands, which arise from the sample substrate and IR windows of the SPECTRAL high-vacuum chamber. This correction is necessary since CVD diamond strongly absorbs between 2300 and 2000 cm^{-1} . However, between the submillimeter and near-IR spectral regions, CVD diamond has excellent throughput, and using diamond transmission windows allows for automatic transitioning across the far- and mid-IR spectral regions while keeping the purge and experimental conditions intact. Thus, for each temperature, far- and mid-IR spectra can be recorded consecutively in the exact same experimental conditions. Prior to vapor deposition, background spectra were collected for each selected temperature. Ice absorption spectra were then recorded and automatically background corrected, i.e., the

³ The annealing process involves depositing the vapor onto the cold substrate in the amorphous phase at very low temperatures (e.g., $< 100 \text{ K}$), then warming the ice to its appropriate crystalline temperature, and annealing it for several hours at this temperature to allow the molecules to adopt a low-energy configuration. Subsequent cooling/warming of the ice is then achieved to record the IR absorbance or transmission spectrum at the required temperature.

single-beam spectrum I of the ice sample deposited on the window was ratioed against the single-beam spectrum I₀ obtained with the chamber IR windows but without the ice sample. This background correction also allowed to remove spectral features introduced by the spectrometer and the remaining traces of ambient atmospheric gases (while continuously purging the IR spectrometer compartments with dried compressed air). The absorption spectrum was then converted to absorbance.

Each laboratory-acquired IR absorbance spectrum shown in this paper was corrected to remove the channel fringes that are produced by the reflections at the vacuum-ice and ice-substrate sample surface (Hirschfeld & Mantz 1976). When removing the channel fringes from the spectrum, the absorbance value was purposely “zeroed in” in the far-IR region for frequencies below 100 cm^{-1} when the signal-to-noise ratio (S/N) becomes low ($S/N < 3$) and the peaks cannot be considered real absorption bands. Due to the high noise level at the low wavenumber end between 50 and 100 cm^{-1} , all wavenumbers below 100 cm^{-1} were then set at the 100 cm^{-1} value for generating the corrected absorbance spectra as well as for computing the optical constants n and k .

After the channel fringes were removed, the corresponding n and k values were computed for each corrected absorbance spectrum. A detailed procedure for computing the optical constants is described in Anderson et al. (2018a, Section 4.3). In summary, we monitored the C_6H_6 thin ice films as they grew with deposition time via double laser interferometry, and then we used the Bragg’s Equation to compute the thickness d (see, e.g., Tempelmeyer & Mills 1968; Domingo et al. 2007); an n_0 of 1.54 at 632.8 nm was adopted from Romanescu et al. (2010). We then estimated the imaginary part of the refractive index (k) from the relation $k(\nu) = \alpha(\nu)/4\pi\nu$, where the Lambert absorption coefficient $\alpha(\nu)$ was initially estimated from the relation $-(\ln T)/d$; T is the ice sample fringe-corrected transmittance spectrum, d is the total ice thickness, and ν is the wavenumber in cm^{-1} . Once the estimated k values were computed, we then employed the Kramers–Kronig relationship to calculate the initial estimate of the real part of the refractive index (n) as a function of wavenumber. The initial estimates of both $n(\nu)$ and $k(\nu)$ were then input into the fully expanded Lambert absorption coefficient equation to compute $\alpha(\nu)$ (see also Rocha & Pilling 2014). $\alpha(\nu)$ was then input back into $k(\nu) = \alpha(\nu)/4\pi\nu$ to compute the new $k(\nu)$ values, and we continued to iteratively adjust the values of $k(\nu)$ to compute the new $n(\nu)$ values until the $n(\nu)$ and $k(\nu)$ values converged to their final states.

All of the original data files of the optical constants as well as the absorbance spectra obtained in this study for C_6H_6 ice at different deposition temperatures will be made available on the NASA website <https://science.gsfc.nasa.gov/691/spicelab>.

3. Experimental C_6H_6 Ice Spectra

Benzene ice was studied from the amorphous to the crystalline phase and we examined the variation of the C_6H_6 ice absorption bands, from the far- to mid-IR spectral region, at deposition temperatures ranging from 15 to 150 K. This study was performed in an effort to better understand the C_6H_6 ice phase transitions with the corresponding observed spectral changes, and to identify when the complete crystallization of benzene ice is achieved. Specifically, we have recorded absorbance spectra at the deposition temperatures of 15, 30, 32, 35, 45, 60, 90, 100, 110, 120, 125, 130, 135, 140, and 150 K (Figures 2–7). We have also

studied the temporal variations of the C_6H_6 ice absorption bands, i.e., the time evolution of the C_6H_6 ice spectra after vapor deposition for each deposition temperature cited earlier. Contrary to our previous results on propionitrile ice (Nna-Mvondo et al. 2019), we did not observe any temporal variation of the C_6H_6 ice band positions, nor any variation in the band intensities and shapes for any of the C_6H_6 absorption bands at any given temperature, even 24 hr after deposition. Therefore, in this paper we only present the results for C_6H_6 ice spectra obtained at different deposition temperatures.

The absorption bands of C_6H_6 ice were assigned in the full far- to mid-IR spectral range studied in this work ($50\text{--}8000\text{ cm}^{-1}$; $200\text{--}1.25\text{ }\mu\text{m}$), based on previous spectral studies of benzene in its liquid, gas, and solid phases (Mair & Hornig 1949; Miani et al. 2000; Bertie & Keefe 2004). Over the last few decades, experimental and theoretical investigations of the vibrational modes of benzene have become increasingly complete due to refined laboratory techniques and increased computational power. The vibrational modes of benzene have been extensively studied so that we were able to assign most of them in our experimental C_6H_6 ice IR spectra. All of the vibrational assignments observed in the C_6H_6 ice IR spectra that we recorded in our laboratory are listed in Table 1, for the amorphous and crystalline phases of benzene ice, deposited at 15 and 130 K, respectively. The vibrational mode assignments are numbered according to Herzberg’s notation (Herzberg 1945). We have considered with confidence spectral peaks in the IR spectra with signals rising above the 3σ noise level as C_6H_6 ice absorption bands. Spectral features with a low S/N (< 3) were disregarded. Apart from the assignment of the $2\nu_{\text{CH}}$ first overtone mode at 5980 cm^{-1} (at 15 K), it was not possible to assign all other spectral features above 4600 cm^{-1} because, at these higher wavenumbers, anharmonic effects are so large that local-mode (LM) analysis is required (Bertie & Keefe 2004; Wyatt 1998). The LM analysis technique is usually developed to describe multiple-quantum (overtone) transitions where vibrational energy tends to become localized on a single bond. It differs from the normal-mode (NM) analysis of vibrations in polyatomic molecules that describes single-quantum transitions.

The benzene molecule belongs to the point group D_{6h} . It has a six-fold axis of symmetry (C_6) along a line through the center of the molecule and perpendicular to the plane of the paper, six vertical planes of symmetry (σ_v) through C_6 at angles of 30° to one another, and one horizontal plane of symmetry (σ_h) perpendicular to C_6 . C_6H_6 has 12 different symmetry types (species) (A_{1g} , A_{1u} , A_{2g} , A_{2u} , B_{1g} , B_{1u} , B_{2g} , B_{2u} , E_{1g} , E_{1u} , E_{2g} , and E_{2u}) and 20 fundamental vibrations (see Table 1), which were all detected in the C_6H_6 ice spectra that we recorded from 15 to 130 K: $\nu_1(A_{1g})$, $\nu_2(A_{1g})$, $\nu_3(A_{2g})$, $\nu_4(A_{2u})$, $\nu_5(B_{1u})$, $\nu_6(B_{1u})$, $\nu_7(B_{2g})$, $\nu_8(B_{2g})$, $\nu_9(B_{2u})$, $\nu_{10}(B_{2u})$, $\nu_{11}(E_{1g})$, $\nu_{12}(E_{1u})$, $\nu_{13}(E_{1u})$, $\nu_{14}(E_{1u})$, $\nu_{15}(E_{2g})$, $\nu_{16}(E_{2g})$, $\nu_{17}(E_{2g})$, $\nu_{18}(E_{2g})$, $\nu_{19}(E_{2u})$, and $\nu_{20}(E_{2u})$.

In the next sections, we describe and analyze in detail the IR absorbance spectra of benzene ice obtained in this study⁴ and their evolution with temperature; Section 3.1 details in the

⁴ The raw spectra were recorded with the software of the FTIR spectrometer sets for collecting data at 4 cm^{-1} resolution; however, the default/standard configuration for normal work for a resolution of 4 cm^{-1} , with a zero-filling factor of two, sets the data spacing automatically at 2 cm^{-1} , i.e., the spectra are automatically oversampled by a factor of two in the standard configuration. The IR spectra displayed in figures are all shown in the default configuration as collected initially, i.e., with wavenumber spaced by 2 cm^{-1} (oversampled by two).

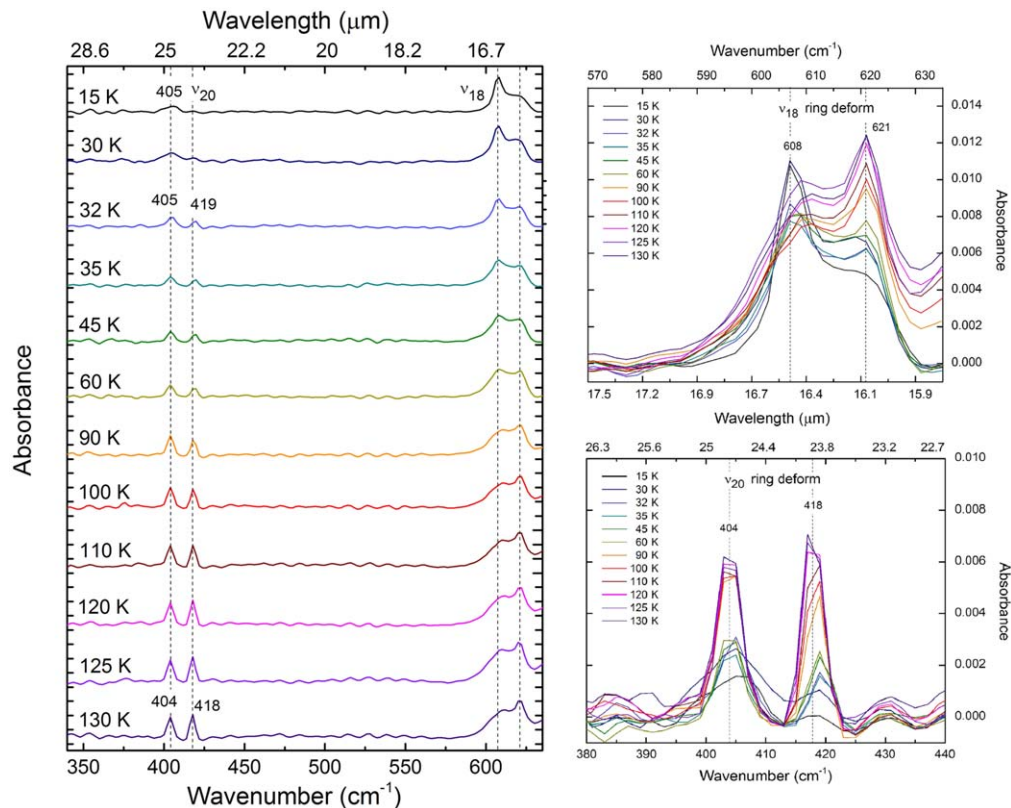


Figure 2. Far-IR absorbance spectra of C_6H_6 ice obtained after deposition of the benzene vapors at temperatures from 15 to 130 K. Thicknesses of ice films at 15, 30, 32, 35, 45, 60, 90, 100, 110, 120, 125, and 130 K were 3.87, 3.82, 3.92, 3.70, 4.08, 3.70, 3.71, 3.59, 3.63, 3.42, 3.69, and 3.63 μm , respectively. The left panel shows the entire absorbance spectra from 340 to 635 cm^{-1} (29.4–15.7 μm). The panels on the right depict specific spectral regions of C_6H_6 ring deformation modes, the ν_{18} band (in the upper panel) and the ν_{20} band (in the lower panel). Superimposed in the panels are the vibrational transitions, and the numbers are peak frequencies in cm^{-1} for the observed ice absorption bands.

far-IR region from 50 to 640 cm^{-1} (100–15.6 μm), and Section 3.2 describes in the mid-IR region from 640 to 8000 cm^{-1} (15.6–1.25 μm).

3.1. Far-IR C_6H_6 Ice Spectra (50 to 640 cm^{-1})

Figure 2 shows C_6H_6 ice far-IR spectra obtained in our laboratory for benzene vapors deposited at temperatures between 15 and 130 K. Even though we carried out experiments at higher temperatures (135, 140, and 150 K), we observed that at temperatures higher than 130 K, C_6H_6 ice sublimates under the experimental conditions of the SPECTRAL chamber, in which a vacuum pressure is constantly maintained at 10^{-8} mbar during the vapor deposition, and the recording of the IR spectra. Thus, in this article we present the experimental results for $T_d \leq 130$ K.

The far-IR spectral region between 50 and 400 cm^{-1} (100–25 μm) did not display any absorption bands of benzene ice defined as detectable (spectral features with an $S/N > 3$), for any of the deposition temperatures at which the spectra were collected. In this low-frequency range, several absorption bands between 55 and 130 cm^{-1} have been previously assigned to vibrations characteristic of the crystal lattice. These torsional lattice vibrations, which correspond to out-of-plane and in-phase librations of all benzene molecules about the three crystal axes, are IR- and Raman-active. They have been previously observed in Raman spectra of solid benzene (Epstein & Steiner 1934; Bonadeo et al. 1972; Ishii et al. 1996), as well in the far-IR spectra of crystalline C_6H_6 at 173 K (Chantry et al. 1967), 138 K (Harada & Shimanouchi 1967), 100 K (Harada & Shimanouchi 1971),

and from 15 to 150 K (Sataty et al. 1973; Sataty & Ron 1976). We did not identify any of these absorption bands in our experimental far-IR spectra, even for thicker ice films (10 μm), since the signal in this low-energy far-IR spectral region has a low spectral resolution (due the intense noise produced by our FTIR spectrometer below 100 cm^{-1}). Thus, our experimental system and procedure did not allow us to distinguish them. Bertie & Keefe (2004) reported very weak bands at 264 and 301.6 cm^{-1} for liquid benzene at 25°C. With our FTIR instrument and experimental protocol, we were able to detect absorption bands at this frequency range (with absorbance height as low as 0.002 absorbance unit for $S/N > 3$); for example, we detected the weak far-IR absorption bands of propionitrile between 100 and 390 cm^{-1} (Anderson et al. 2018a; Nna-Mvondo et al. 2019). This was not the case for C_6H_6 ice. Very possibly, the bands of liquid C_6H_6 measured between 100 and 300 cm^{-1} are very weak bands with intensity below the noise level of our spectra.

At frequencies higher than 400 cm^{-1} , two vibrational modes of C_6H_6 ice, the ν_{20} and ν_{18} ring deformation bands, were detected as shown in Figure 2 and listed in Table 1. For both vibrational modes, we observed spectral variations with the deposition temperature involving significant changes in absorption band position, intensity, and shape (Figure 2).

At 15 and 30 K, the ν_{20} ring deformation mode peaks at 405 and 404 cm^{-1} , respectively, and appears as a broad band. From 32 K and higher, this band is split into an asymmetrical doublet. At 32 K, the ν_{20} doublet-band branches at 405 and 419 cm^{-1} , with the first maximum at 405 cm^{-1} more intense than the second maximum at 419 cm^{-1} . With increasing

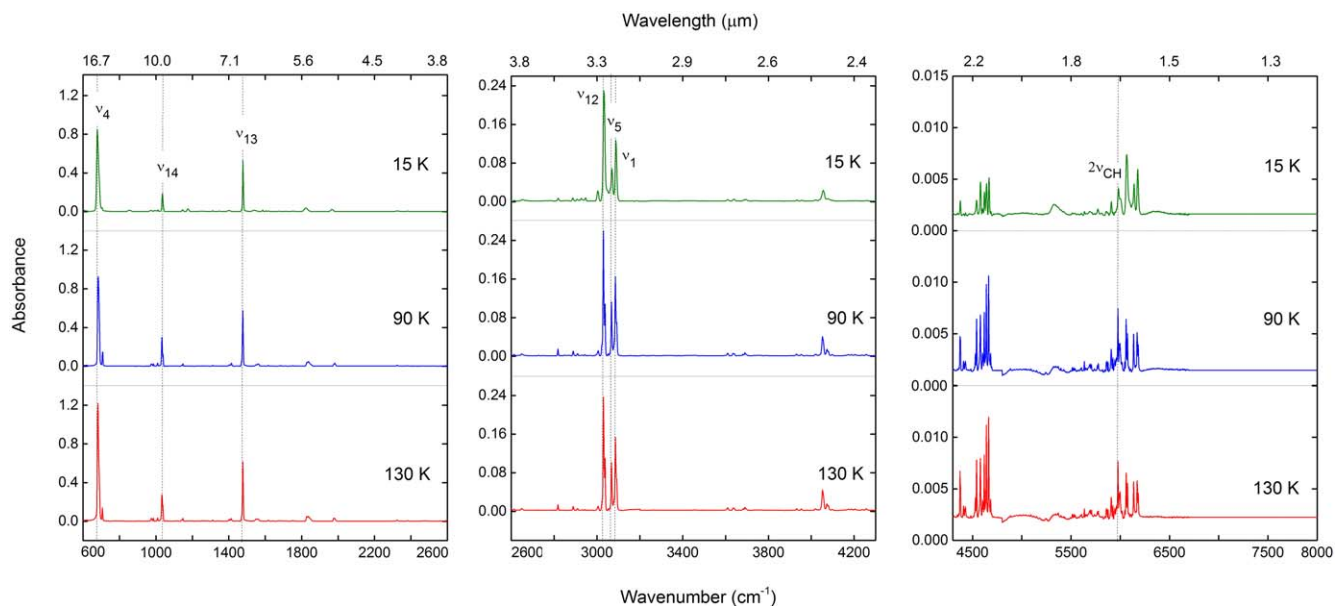


Figure 3. Full-range mid-IR absorbance spectra of C_6H_6 ice obtained after deposition of the benzene vapors at temperatures of 15, 90, and 130 K (thin ice films of 3.87, 3.71, and 3.63 μm , respectively).

deposition temperature, the ν_{20} doublet increases in intensity and in the splitting, and shifts slightly to lower energies (Figure 2). At 110 K, the doublet is symmetrical, with an equalization of the intensities of the doublet, but from 120 K and higher, the two maxima reverse in intensity with the second maximum more intense than the first one. At 130 K, the doublet is shifted by 1 cm^{-1} and peaks at 404 and 418 cm^{-1} .

The ν_{18} ring deformation mode of C_6H_6 ice also undergoes significant spectral changes with the deposition temperature (Figure 2). The band appears as a doublet with a main maximum and an inflection at all deposition temperatures, but is poorly resolved compared to the ν_{20} absorption band, which appears with two distinct maxima. At 15 K, the main maximum peaks at about 608 cm^{-1} and the inflection at about 615 cm^{-1} . With increasing deposition temperature, the maximum of the main band weakens and displaces toward higher frequencies. At 90 K, the maximum is relocated at 621 cm^{-1} , thus undergoing a shift of 13 cm^{-1} to higher energies. No further shift of the maximum is observed at higher deposition temperatures, but its intensity at 621 cm^{-1} increases with temperature.

3.2. Mid-IR C_6H_6 Ice Spectra ($640\text{ to }8000\text{ cm}^{-1}$)

Figure 3 displays the mid-IR spectra of benzene ice that we have obtained for deposition temperatures ranging from 15 to 130 K.

Just like the liquid and gas phases, the mid-IR spectra of C_6H_6 ice (Figure 3) depict four C–H stretching modes (ν_1 , ν_5 , ν_{12} and ν_{15}), four C–C stretching modes (ν_2 , ν_9 , ν_{13} , ν_{16}), four C–H symmetric (in-plane) bending modes (ν_3 , ν_{10} , ν_{14} , ν_{17}), four C–H asymmetric (out-of-plane) bending modes (ν_4 , ν_7 , ν_{11} , ν_{19}), and one C–C symmetric bending mode (ν_6), among the 30 molecular normal modes of vibration of benzene, which produce 20 different frequencies (see Table 1). Most of the fundamental vibrations of benzene ice are observed between $650\text{ and }1600\text{ cm}^{-1}$ (Figures 3–5). From $1600\text{ to }6200\text{ cm}^{-1}$, the C_6H_6 ice spectrum is dominated by weak combination

bands, and only the four fundamental C–H stretching vibrational modes ν_1 , ν_5 , ν_{12} , and ν_{15} are detected between $3000\text{ and }3090\text{ cm}^{-1}$ (Figures 3 and 4). In the spectral region $6200\text{--}8000\text{ cm}^{-1}$ ($1.61\text{--}1.25\text{ }\mu m$), for ice film thicknesses ranging from 3.6 to $4.1\text{ }\mu m$, benzene ice does not show any absorption bands (Figure 3).

We mention that there were no C_6H_6 ice absorption bands detected between $1940\text{ and }2300\text{ cm}^{-1}$ due to the intense absorption of the diamond, which is the optical material of the sample substrate and IR windows. Even when the parameters of the FTIR spectrometer were optimized to reduce the intensity of the diamond bands, the mid-IR region between $1940\text{ and }2300\text{ cm}^{-1}$ still showed intense absorption bands of the diamond. As a result, in the fringe-corrected mid-IR spectra shown in Figure 3, the diamond absorption bands were removed by averaging the absorbance values around $1860\text{ and }1950\text{ cm}^{-1}$ and maintaining this averaged value constant at all wavenumbers in between. Similarly, this approach was applied to the wavenumbers between $2000\text{ and }2300\text{ cm}^{-1}$.

As with the far-IR region, the mid-IR spectra of C_6H_6 ice revealed spectral variations with deposition temperature and significant changes in the position, intensity, and shape of the absorption bands, as displayed in Figures 4–7.

Figure 4 represents the spectral regions in the mid-IR of the most intense fundamental vibrational modes of benzene ice and their evolution with the deposition temperature. Every fundamental mode revealed a different spectral behavior with temperature. The ν_4 C–H out-of-plane bending mode (wag vibration), which is the most intense vibrational band of C_6H_6 ice, peaks at 679 cm^{-1} at 15 K. As the temperature increases, it becomes sharper (the FWHM is reduced by 4 cm^{-1} from 15 to 130 K) with an increase in band intensity and shifts to higher energies. At 125 K, the position and intensity of the band stabilize and are shifted by 2 cm^{-1} peaking at 681 cm^{-1} at 125 and 130 K. Surprisingly, the largest shift toward the highest frequencies is not observed at the highest temperature but at 60 and 90 K, with a displacement of 5 cm^{-1} from the band position at 15 K. The weak ν_8 ring deformation mode at

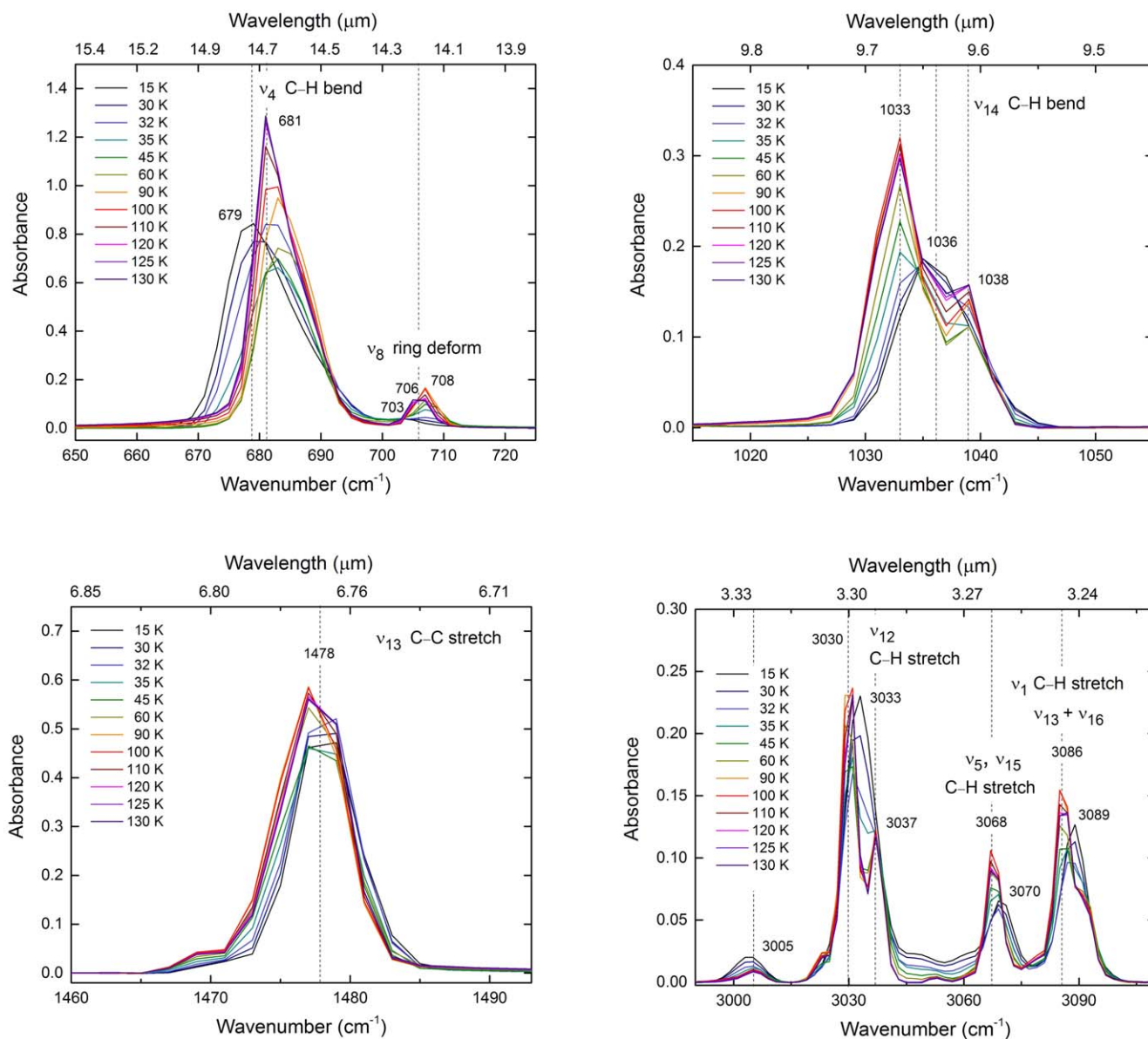


Figure 4. The most intense fundamental modes of C_6H_6 ice in the mid-IR region from absorbance spectra obtained after deposition of the benzene vapors at temperatures from 15 to 130 K. Ice film thickness ranges between 3.6 and 4.1 μm (all thickness values are listed in the caption of Figure 2).

703 cm^{-1} at 15 K undergoes a similar spectral evolution with temperature as with the ν_4 vibrational band; although, the largest spectral shift occurs at lower temperatures between 35 and 60 K, and the band reaches a maximum intensity at 90 and 100 K. The intense ν_{13} C-C stretching mode of C_6H_6 ice at 1478 cm^{-1} does not undergo significant spectral changes with temperature, but only a slight increase in band intensity and, at 90 and 100 K, a small shift of about 0.5 cm^{-1} toward lower energies are observed. Additionally, a small shoulder around 1470 cm^{-1} is growing with increasing temperature. One possible explanation for this shoulder is that at 4 cm^{-1} spectral resolution, some of the vibrational bands are not fully resolved, and some side peaks may appear as a shoulder if positioned at less than the spectral resolution from the main band. The ν_{14} C-H in-plane bending mode is another intense absorption band of C_6H_6 ice. It peaks as a singlet band at 1036 cm^{-1} at 15 K and starts to split in two at 32 K to become an asymmetric doublet at 60 K. From 125 K, the doublet is stable and has an intense maximum at 1033 cm^{-1} and a second weaker

maximum at 1038 cm^{-1} . The four C-H stretching modes ν_1 , ν_5 , ν_{12} , and ν_{15} of C_6H_6 ice observed between 3000 and 3090 cm^{-1} evolve distinctly with deposition temperature. The ν_{12} mode at 3033 cm^{-1} at 15 K has a similar behavior as the ν_{14} band. It splits into two maxima as the temperature increases, which stabilize from 125 K and form an asymmetric doublet peaking at an intense maximum at 3031 cm^{-1} , and another one at 3037 cm^{-1} . Like for the ν_{13} band, a growing shoulder with increasing temperatures is observed at a higher energy around 3023 cm^{-1} . The main spectral changes for the ν_1 , ν_5 , and ν_{15} absorption bands are a shift to lower energies of 3 and 2 cm^{-1} , respectively, from 15 to 130 K and an increase in the band intensity. A small inflection starts to appear in the ν_1 stretch band at 45 K but never achieves a resolved doublet with maxima. As for the ν_{12} vibrational mode, from 125 K, no more spectral changes are observed for the ν_1 , ν_5 , and ν_{15} stretch bands.

Figure 5 displays how the other 10 C_6H_6 ice fundamental vibrational modes (ν_2 , ν_3 , ν_6 , ν_7 , ν_9 , ν_{10} , ν_{11} , ν_{16} , ν_{17} , and ν_{19})

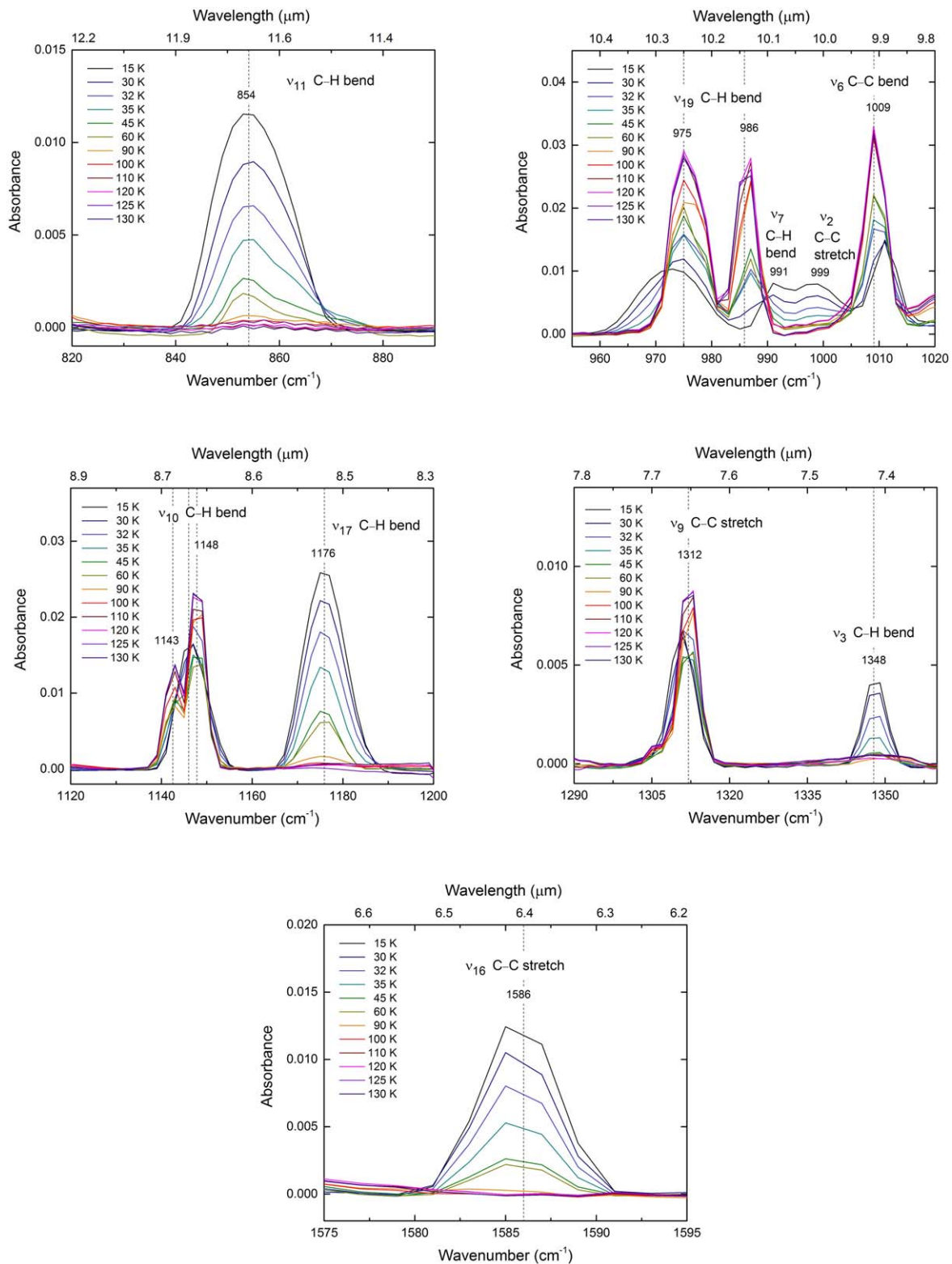


Figure 5. Other fundamental modes of C_6H_6 ice in the mid-IR region from absorbance spectra obtained after deposition of the benzene vapors at temperatures from 15 to 130 K. Ice film thickness ranges between 3.6 and 4.1 μm (all thickness values are listed in the caption of Figure 2).

evolve with deposition temperature. These vibrations are much weaker in intensity than the fundamentals described above. The major result for this set of vibrational bands is the disappearance of several modes as the deposition temperature increases. This is the case for the ν_3 and ν_{17} C-H symmetric bending modes, the ν_7 and ν_{11} wagging vibrations, the ν_2 , and

ν_{16} C-C stretching modes, whose bands peak at 1348, 1176, 991, 854, 999, and 1586 cm^{-1} at 15 K, respectively. At temperatures higher than 15 K, these absorption bands decrease in intensity to disappear completely from 100 K. These specific vibrational modes are highly symmetric inactive modes in C_6H_6 gas. They are activated by the disorder of the asymmetric

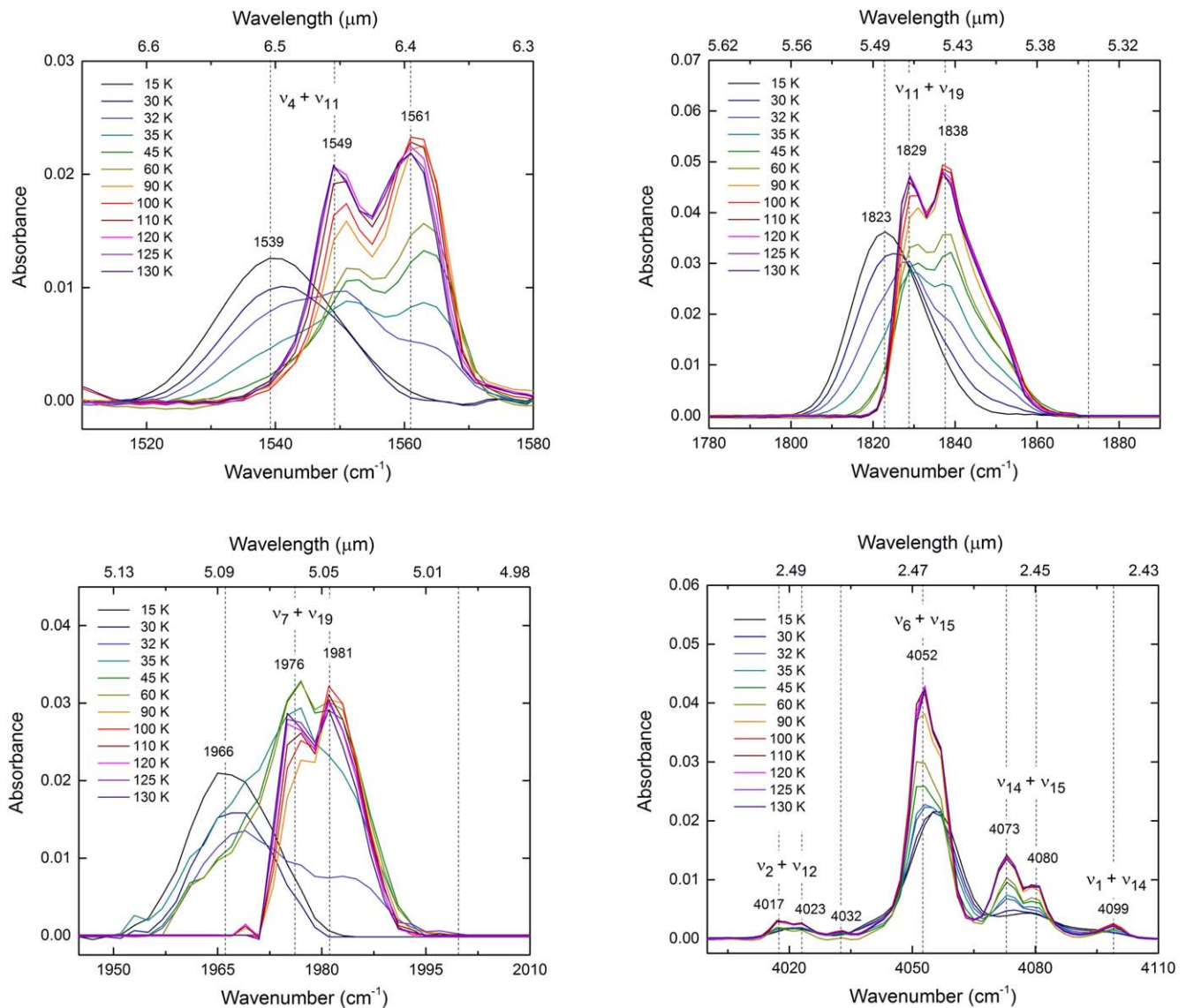


Figure 6. The most intense combination modes of C_6H_6 ice in the mid-IR region from absorbance spectra obtained after deposition of the benzene vapors at temperatures from 15 to 130 K. Ice film thickness ranges between 3.6 and 4.1 μm (all thickness values are listed in the caption of Figure 2).

environment of the amorphous phase, and then turn highly symmetric, again, in the ordered crystalline phase. Consequently, we identify this significant spectral change as an indication of the ongoing crystallization of the C_6H_6 ice phase.

The four other fundamental vibrations ν_6 , ν_9 , ν_{10} , and ν_{19} display different spectral changes with the deposition temperature. The ν_6 C–C symmetric bending modes and the ν_9 C–C stretching bands, which peak at 1011 and 1311 cm^{-1} at 15 K, respectively, increase in intensity as the temperature increases, and they reach a maximum intensity between 120–130 K. Between 15 and 130 K, the vibrational modes ν_6 and ν_9 shift to lower energies by 2 cm^{-1} and to higher energies by 1 cm^{-1} , respectively. A small shoulder in the ν_9 appears from 90 to 130 K. The ν_{10} C–H in-plane bending mode peaks at 1146 cm^{-1} at 15 K and splits into two maxima from 45 K. At 130 K, the asymmetric doublet has maxima at 1143 and 1148 cm^{-1} .

The mid-IR spectra of C_6H_6 ice display a large number of binary to quaternary combination bands (Table 1). Several of the combination bands, for which a large number of

combinations is possible, have no spectral assignment, especially for the spectral region between 4550 and 6200 cm^{-1} . Figure 6 shows the four most intense combination bands and their temperature dependences. The remaining combination bands observed in the C_6H_6 ice spectra are very weak in intensity. As for the absorption bands presented in Figure 6, all of the combination modes change markedly with the temperature. As the deposition temperature increases, several of them undergo splitting into two to four components with an increase in the band intensity and a frequency shift, as seen in Figure 6. While few of them experience a spectral shift to higher energies, like the three most intense combination bands at 1539 cm^{-1} , 1823 cm^{-1} , and 1966 cm^{-1} at 15 K, the other combination modes displace to lower frequencies, as does the band at 4056 cm^{-1} (Figure 6). At frequencies higher than 3620 cm^{-1} , all combination modes have a band shift toward lower energies.

In the very high-frequency region of the benzene ice spectra (frequencies higher than 5000 cm^{-1}), we observe the first overtone $2\nu_{CH}$ of the C–H stretching vibrations (Figure 7).

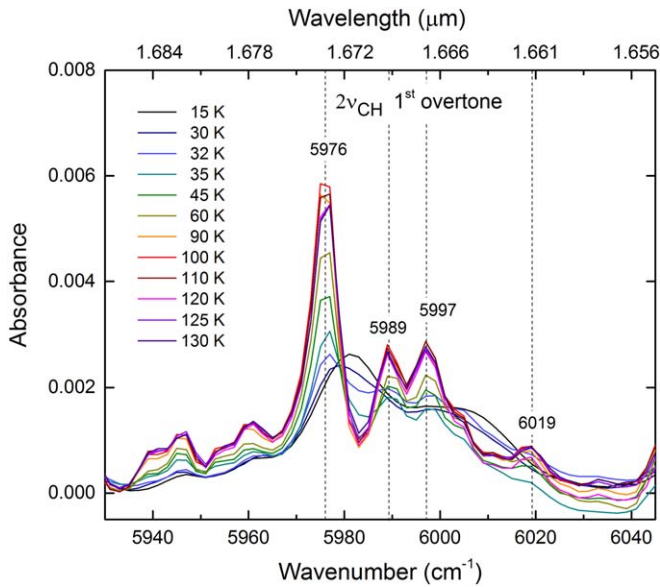


Figure 7. First overtone ($2\nu_{\text{CH}}$) of the C–H stretching vibrations of C_6H_6 ice from absorbance spectra obtained after deposition of the benzene vapors at temperatures from 15 to 130 K. Ice film thickness ranges between 3.6 and 4.1 μm (all thickness values are listed in the caption of Figure 2).

This very weak overtone mode appears as a broad band at 15 K, which peaks at 5980 cm^{-1} and splits into several components as the temperature increases, with a main maximum at 5976 cm^{-1} at 130 K.

3.3. Identification of C_6H_6 Ice Phases from the Experimental IR Spectra

As described in Sections 3.1 and 3.2, the far- and mid-IR absorbance spectra of benzene ice reveal several temperature-dependent spectral changes. Except for the ν_{13} C–C stretching mode at 1478 cm^{-1} , all of the C_6H_6 ice vibrational modes are modified when C_6H_6 vapor is deposited at different temperatures. The increase of the deposition temperature from 15 to 130 K triggers band sharpening and/or band splitting, an increase in band intensity, and shifts in band position. Additionally, as noted in Section 3.2, some C_6H_6 ice absorption bands at 15 K disappear at temperatures $\geq 100\text{ K}$ and thus behave as IR-inactive in the crystal. This temperature-dependent behavior evidences the transition of C_6H_6 ice from the amorphous to crystalline phase, as generally observed for ices studied in the laboratory. In our experiments, we identify the amorphous phase of C_6H_6 ice at 15 and 30 K for which the IR spectra present only singlet vibrational bands that do not undergo any frequency shift. From 32 K, we notice that various spectral changes are initiated. In the far-IR spectral region, the behavior of the ν_{20} ring deformation mode of C_6H_6 ice, which changes from a broad singlet at 15 and 30 K to a doublet at 32 K, is a strong indication that the molecules of C_6H_6 ice start to order. In the mid-IR region, several fundamental vibrational modes and combination modes start to split at 32 K (appearance of a shoulder or inflection in the bands). From 32 to 120 K, the far- and mid-IR vibrational bands of benzene ice evolve significantly with the temperature and produce distinct transitions in the spectra that illustrate the ongoing reordering of the molecules toward a lower energy state. From 120 to 130 K, C_6H_6 ice absorption bands do not undergo any further spectral changes, resulting in identical IR spectra and

indicating that the ordering and crystal orientations of C_6H_6 ice molecules are complete. At temperatures higher than 130 K, the ice samples sublime, which alters the mid- and far-IR spectra with a decrease in the intensity of all C_6H_6 absorption bands.

A previous laboratory study on benzene ice, directly deposited at low temperatures from 13 to 78 K or annealed up to 96 K, reports a transition in the ice phase from amorphous to crystalline from around 60 K using Raman spectroscopy and X-ray diffraction (Ishii et al. 1996). Ishii et al. (1996) reported no significant change in the Raman spectra and diffraction patterns for temperatures lower than 60 K, and they defined the C_6H_6 ice crystallization temperature around 60 K. Mouzay et al. (2021), after depositing at 16 K and warming it up to 300 K, observe the evolution of the surface coverage of the ν_{13} and ν_{14} vibrational modes of C_6H_6 ice with temperature, and report similarly benzene crystallization at around 55 K. Hollenberg & Dows (1962) characterized C_6H_6 ice at 85 K as crystalline. On the other hand, differential thermal analyses of benzene have determined the glass transition temperature of benzene to be at 120 K (Dubochet et al. 1984) or at 130 K (Angell et al. 1978). And results from nuclear magnetic resonance absorption spectroscopy of solid C_6H_6 from 75 to 278 K have identified that the reorientation of C_6H_6 molecules about their six axes is initiated at about 90 K (Andrew & Eades 1953). In the present study, we assessed the crystalline temperature (i.e., the temperature at which crystallization is completely achieved) based on two criteria: (1) there are no observed changes (or almost no changes) in the strength and/or spectral dependence of the IR absorption bands after an increase in the deposition temperature, and (2) there is no noticeable sublimation of the ice film at the temperature held after vapor deposition. Based on these criteria and on our results of the temperature dependence of the far- and mid-IR spectra of benzene ice, we have identified that C_6H_6 ice has completed crystallization at the deposition temperature (T_d) determined as $120\text{ K} \leq T_d \leq 130\text{ K}$. This result is compatible with the glass transition temperatures previously estimated. For this confined temperature range, the crystalline phase of benzene ice is unambiguously identified from the disordered amorphous and ordering transition phases.

3.4. Optical Constants of Amorphous and Crystalline C_6H_6 Ices

Figure 8 displays the real (n) and imaginary (k) parts of the ice complex refractive index of benzene ice in the far- and mid-IR from 50 to 8000 cm^{-1} ($200\text{--}1.25\ \mu\text{m}$). We calculated n and k from our laboratory spectra at each temperature from 15 to 130 K, and using n_0 value of 1.54 ± 0.02 determined by Romanescu et al. (2010). The complex indices of refraction of C_6H_6 ice can be used to determine absorption cross-sectional spectra, which can be compared with astronomical emission spectra. We are the first to report cryogenic measurements of n and k of C_6H_6 ice at a variety of temperatures in both the amorphous and crystalline phases. We observe that n and k vary with the temperature (Figures 8 and 9).

In Figure 9, we illustrate the spectral dependence of n and k for the most intense vibrational mode of C_6H_6 ice, the ν_4 C–H asymmetric bending mode, in the amorphous phase at 15 K (black curve) and in the crystalline phase at 130 K (red curve).

Table 1
IR Vibrational Modes and Frequencies of Amorphous and Crystalline C₆H₆ Ices from the Laboratory Spectra Obtained in This Study

Amorphous (15 K) IR Frequencies (cm ⁻¹) ^a	Crystalline (130 K) IR Frequencies (cm ⁻¹) ^a	Band Assignment ^b	References ^c
405 vw	404 vw ^d 418 vw ^d	ν_{20} ring deform.	<i>b, c</i>
608 vw ^d 619 vw ^d	611 vw ^d 621 vw ^d	ν_{18} ring deform.	<i>c</i>
679 vs	681 vs	ν_4 C-H asym. bending	<i>a, b, c</i>
703 vw	706 <i>m</i>	ν_8 ring deform.	<i>a, b, c</i>
S/N < 3 ^c	785 vvw	$\nu_{17} - \nu_{20}$	<i>b</i>
854 w	— ^f	ν_{11} C-H asym. bending	<i>a, b, c</i>
973 w	975 w 986 w	ν_{19} C-H asym. bending	<i>a, b, c</i>
991 vw	— ^f	ν_7 C-H asym. bending	<i>b, c</i>
999 vw	— ^f	ν_2 C-C stretching	<i>a, c</i>
1011 vw	1009 vw	ν_6 C-C sym. bending	<i>a, b, c</i>
1036 <i>s</i>	1033 <i>s</i> ^d 1038 <i>s</i> ^d	ν_{14} C-H sym. bending	<i>a, b, c</i>
S/N < 3 ^c	1109 vw ^d 1119 vw ^d	$\nu_8 + \nu_{20}$	<i>a, b</i>
1146 w	1143 w ^d 1148 w ^d	ν_{10} C-H sym. bending	<i>a, b, c</i>
1176 w	— ^f	ν_{17} C-H sym. bending	<i>a, b, c</i>
1243 vw 1256 vw	1250 vw ^d 1259 vw ^d 1268 vw ^d 1277 vw ^d	$\nu_{10} + \nu_{16}$	<i>a, b</i>
1311 vw	1312 vw	ν_9 C-C stretching	<i>a, b, c</i>
1348 vw	— ^f	ν_3 C-H sym. bending	<i>a, b, c</i>
1399 vw	1402 vw ^d 1413 vw ^d	$\nu_7 + \nu_{20}$	<i>a, b</i>
1478 vs	1478 vs	ν_{13} C-C stretching	<i>a, b, c</i>
1539 w	1549 w ^d 1561 w ^d	$\nu_4 + \nu_{11}$	<i>a, b</i>
1586 vw	— ^f	ν_{16} C-C stretching	<i>a, b, c</i>
1604 vw	— ^f	$\nu_2 + \nu_{18}$	<i>a, b</i>
1617 vw	1617 vw	$\nu_6 + \nu_{18}$	<i>a, b</i>
S/N < 3 ^c	1644 vw	$\nu_{14} + \nu_{18}$	<i>a, b</i>
1672 vw	1679 vw ^d 1684 vw ^d	$\nu_8 + \nu_{19}$	<i>a, b</i>
1713 vw	1714 vw	$\nu_6 + \nu_8$	<i>a, b</i>
1754 vw	1754 vw	$\nu_{10} + \nu_{18}$	<i>a, b</i>
1823 <i>m</i>	1829 <i>m</i> ^d 1838 <i>m</i> ^d	$\nu_{11} + \nu_{19}$	<i>a, b</i>
1966 w	1976 w ^d 1981 w ^d	$\nu_7 + \nu_{19}$	<i>a, b</i>
2326 vw	2325 vw	$\nu_{10} + \nu_{17}$	<i>a, b</i>
2383 vw	2381 vw	$\nu_3 + \nu_{14}$	<i>a, b</i>
S/N < 3 ^c	2466 vw 2482 vw 2490 vw	$\nu_9 + \nu_{17}$	<i>b</i>
2594 vw	2592 vw	$\nu_6 + \nu_{16}$	<i>a, b</i>
2613 vw	2612 vw	$\nu_6 + (\nu_{16} + \nu_{18})$	<i>b</i>
2651 vw	2648 vw	$\nu_{13} + \nu_{17}$	<i>a, b</i>
— ^f	2728 vw	$\nu_{10} + \nu_{16}$	<i>b</i>
2783 vw	— ^f	$\nu_{10} + (\nu_2 + \nu_{18})$	<i>b</i>
2819 vw	2818 vw ^d 2831 vw ^d	$\nu_3 + \nu_{13}$	<i>a, b</i>
— ^f	2849 vw	Not assigned	
2887 vw	2889 vw	Not assigned	
2907 vw 2926 vw 2947 vw	2909 vw 2933 vw 2944 vw ^d 2953 vw ^d	$\nu_9 + \nu_{16}$	<i>a, b</i>
3004 vw	3005 vw	Not assigned	
3033 <i>s</i>	3030 <i>s</i> ^d 3037 <i>s</i> ^d	ν_{12} C-H stretching	<i>a, b, c</i>
3070 <i>m</i>	3068 <i>m</i>	ν_5, ν_{15} C-H stretching	<i>a, c</i>
3089 <i>s</i>	3086 <i>s</i>	ν_1 C-H stretch., $\nu_{13} + \nu_{16}$	<i>a, b</i>
3447 vw	3457 vw	$\nu_{15} + \nu_{20}$	<i>a, b</i>
3610 vw	3610 vw	$\nu_5 + \nu_{18}$	<i>a, b</i>
3639 vw	3635 vw ^d 3641 vw ^d	$\nu_{12} + \nu_{18}$	<i>a, b</i>
S/N < 3 ^c	3659 vw	Not assigned	
3684 vw 3694 shoulder	3682 vw ^d 3691 vw ^d	$(\nu_2 + \nu_{13} + \nu_{18}) + \nu_{18}, (\nu_{13} + \nu_{16}) + \nu_{18}$	<i>b, b</i>
3934 vw	3931 vw	$\nu_{11} + \nu_{12}$	<i>a</i>
3955 vw	3953 vw	$\nu_3 + \nu_6 + (\nu_2 + \nu_{18})$	<i>b</i>
4021 vw	4017 vw ^d 4023 vw ^d	$\nu_2 + \nu_{12}$	<i>b</i>
— ^f	4032 vw	Not assigned	
4056 <i>m</i>	4052 <i>m</i>	$\nu_6 + \nu_{15}$	<i>b</i>
4079 vw	4073 vw ^d 4080 vw ^d	$\nu_{14} + \nu_{15}$	<i>b</i>
S/N < 3 ^c	4099 vw	$\nu_1 + \nu_{14}$	<i>b</i>
S/N < 3 ^c	4156 vw	$\nu_{10} + \nu_{15}$	<i>b</i>
4174 vw	4168 vw ^d 4174 vw ^d	$\nu_{10} + \nu_{15}$	<i>a, b</i>
4193 vw	4189 vw	$\nu_{12} + \nu_{17}$	<i>b</i>
S/N < 3 ^c	4203 vw	Not assigned	
S/N < 3 ^c	4237 vw	$\nu_5 + \nu_{17}$	<i>a, b</i>
4258 vw	4256 vw	$\nu_{17} + (\nu_{13} + \nu_{16})$	<i>b</i>
4348 vw	4347 vw	Not assigned	

Table 1
(Continued)

Amorphous (15 K) IR Frequencies (cm ⁻¹) ^a	Crystalline (130 K) IR Frequencies (cm ⁻¹) ^a	Band Assignment ^b	References ^c
4375 <i>vw</i>	4361 <i>vw</i> 4372 <i>vw</i> ^d 4377 <i>vw</i> ^d	$\nu_9 + \nu_{15}, \nu_3 + \nu_{12}$	<i>a, b</i>
4411 <i>vw</i>	4409 <i>vw</i>	$\nu_3 + (\nu_2 + \nu_{13} + \nu_{18})$	<i>b</i>
4429 <i>vw</i>	4423 <i>vw</i> ^d 4428 <i>vw</i> ^d	$\nu_3 + (\nu_{13} + \nu_{16})$	<i>b</i>
S/N < 3 ^e	4481 <i>vw</i>	Not assigned	
4541 <i>vw</i>	4520 <i>vw</i> ^d 4529 <i>vw</i> ^d 4541 <i>vw</i> ^d	$\nu_{13} + \nu_{15}$	<i>b</i>
4581 <i>vw</i>	4580 <i>vw</i>	$\nu_1 + \nu_{13}$	<i>b</i>
4602 <i>vw</i>	4602 <i>vw</i> ^d 4609 <i>vw</i> ^d	Not assigned	
4619 <i>vw</i>	4618 <i>vw</i>	Not assigned	
4641 <i>vw</i>	4640 <i>vw</i>	Not assigned	
4667 <i>vw</i>	4663 <i>vw</i> ^d 4673 <i>vw</i> ^d	Not assigned	
4686 <i>vw</i>	4684 <i>vw</i>	Not assigned	
5326 <i>vw</i>	5345 <i>vw</i>	Not assigned	
S/N < 3 ^e	5513 <i>vw</i>	Not assigned	
S/N < 3 ^e	5530 <i>vw</i>	Not assigned	
S/N < 3 ^e	5542 <i>vw</i>	Not assigned	
S/N < 3 ^e	5605 <i>vw</i>	Not assigned	
5637 <i>vw</i>	5636 <i>vw</i>	Not assigned	
5689 <i>vw</i>	5680 <i>vw</i> ^d 5687 <i>vw</i> ^d 5692 <i>vw</i> ^d 5707 <i>vw</i> ^d	Not assigned	
5773 <i>vw</i>	5768 <i>vw</i> ^d 5777 <i>vw</i> ^d	Not assigned	
S/N < 3 ^e	5858 <i>vw</i> ^d 5864 <i>vw</i> ^d	Not assigned	
S/N < 3 ^e	5877 <i>vw</i>	Not assigned	
5910 <i>vw</i>	5909 <i>vw</i>	Not assigned	
S/N < 3 ^e	5926 <i>vw</i>	Not assigned	
S/N < 3 ^e	5947 <i>vw</i>	Not assigned	
S/N < 3 ^e	5961 <i>vw</i>	Not assigned	
5980 <i>vw</i>	5976 <i>vw</i> ^d 5989 <i>vw</i> ^d 5997 <i>vw</i> ^d 6019 <i>vw</i> ^d	$2\nu_{\text{CH}} 1^{\text{st}}$ overtone (C–H stretch)	<i>b</i>
6066 <i>vw</i>	6047 <i>vw</i> ^d 6061 <i>vw</i> ^d 6074 <i>vw</i> ^d	Not assigned	
6140 <i>vw</i>	6135 <i>vw</i>	Not assigned	
6178 <i>vw</i>	6171 <i>vw</i> ^d 6184 <i>vw</i> ^d	Not assigned	

Notes.^a Intensities of band: *vs* very strong, *s* strong, *m* medium, *w* weak, *vw* very weak, *vwv* very very weak.^b The fundamental vibrations are numbered following Herzberg (1945).^c The band assignments are based on crystalline ice spectral data published in (a) Mair & Hornig (1949) and on liquid and gas phase data reported in (b) Bertie & Keefe (2004) and (c) Miani et al. (2000), respectively. Bertie & Keefe (2004) uses Herzberg notation, while Mair & Hornig (1949) and Miani et al. (2000) follow the notation of Wilson (1934) and Wilson et al. (1955).^d Multiple frequencies that appear for the same vibrational assignment designate a band that is split into two, three, or four.^e Features for which frequencies are not indicated are below three times the noise level (S/N < 3) and therefore are not considered with sufficient confidence as absorption bands of C₆H₆ ice.^f — Non-observed frequencies.**4. Implications for Titan Studies**

As indicated in Section 1, Vinatier et al. (2018) have recently identified benzene ice mixed with other unidentified compounds in Titan’s stratosphere by analyzing Cassini CIRS nadir and limb mid-IR spectra. From limb observations acquired in 2015 March, they detected an ice cloud emission feature peaking at 682 cm⁻¹ at altitudes between 168 and 278 km, and identified solid benzene as the best chemical match of this emission feature. For their study, they used the experimental spectrum of crystalline C₆H₆ ice deposited at 130 K by Schmitt et al. (2015). Specifically, they analyzed the C₆H₆ ν_4 C–H out-of-plane bending mode detected in the IR spectrum of Schmitt et al. (2015), to fit the 682 cm⁻¹ emission feature, and they determined the spectral dependences of the extinction, absorption, and scattering cross sections per unit particle volume of pure C₆H₆ ice. In the Schmitt et al. (2015) experiment, a 1.65 μm thin film of C₆H₆ ice, produced by vapor deposition of C₆H₆ vapors at 130 K, was analyzed in the mid-IR region from 400 to 4200 cm⁻¹ (2.5–2.38 μm). In their mid-IR spectra, the ν_4 C–H out-of-plane bending mode appeared as an asymmetric

doublet band with the two maxima at 679 and 681 cm⁻¹ and a width of ~ 6.5 cm⁻¹. Vinatier et al. (2018) indicated that in the Schmitt et al. (2015) experimental C₆H₆ spectra, the most intense bands of C₆H₆ ice were very weakly sensitive with temperature, with an observed spectral shift < 0.5 cm⁻¹ between 60 and 130 K. We, however, were unable to corroborate this result since we did not find any published work from Schmitt et al. (2015) reporting a study on the spectral and temperature dependence of C₆H₆ ice. From personal communication, we have been acquainted that Schmitt and colleagues carried out this experimental study by condensing C₆H₆ at 130 K and then cooling to temperatures down to 60 K. Our results displayed in Figure 10 differ slightly from data obtained by Schmitt et al. (2015). In our mid-IR spectra, the ν_4 vibrational mode at 130 K appears as a singlet band that is less intense than the doublet observed by Schmitt et al. (2015). In our studies, this band peaks at 681 cm⁻¹ and has a width of ~ 7.5 cm⁻¹ (Figure 10). Mouzay et al. (2021) reported in their C₆H₆ crystalline ice spectra at 130 K also a single band for the ν_4 C–H out-of-plane bending mode, but

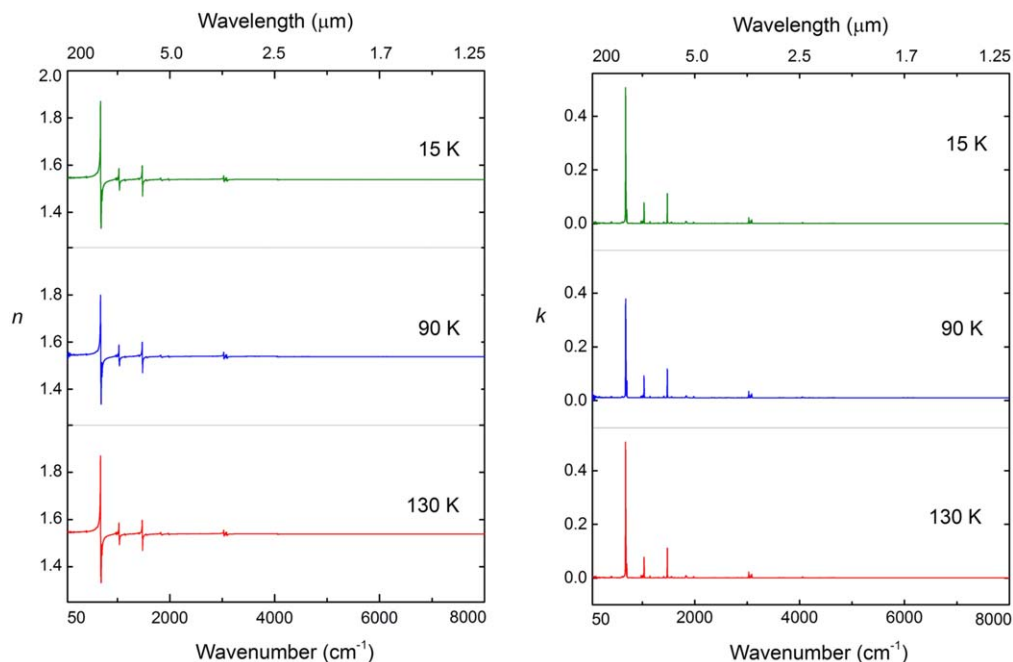


Figure 8. Spectral dependence of the real (n) and imaginary (k) parts of the complex refractive index of C_6H_6 ice at deposition temperatures of 15, 90, and 130 K in the spectral range 50–8000 cm^{-1} (200–1.25 μm). C_6H_6 ice was formed by direct vapor deposition at 15, 90, and 130 K to produce thin ice films of 3.87, 3.71, and 3.63 μm , respectively. n and k were calculated using a custom-developed IDL program that uses the Beer–Lambert law and an iterative Kramers–Kronig analysis of the laboratory corrected absorbance spectra of C_6H_6 ice.

peaking at 679 cm^{-1} . For condensation temperatures from 60 to 130 K, we observe a band displacement of 2 cm^{-1} to higher energies and also that the ν_4 vibrational mode is temperature dependent (Figure 4). As pointed out in Section 3.2, we observe that as the condensation temperature increases, the ν_4 band becomes sharper with an increase in band intensity and shifts to higher energies.

Mouzay et al. (2021) showed that the ν_4 vibrational mode is shifted to higher frequencies from 16 to 130 K by 5 cm^{-1} , but, contrarily to our results, its shape looks almost identical. And after depositing the vapor of C_6H_6 onto a gold-plated substrate at 130 K, keeping at 130 K for a few hours and finally cooling down to 70 K, no significant frequency shift in the ν_4 band is observed with temperature. The band intensity varies very slightly from 70 to 130 K.

The discrepancies in temperature dependences between our spectral results, those of B. Schmitt et al. (unpublished work), and those of Mouzay et al. (2021) certainly result in the fact that we have studied IR spectra of C_6H_6 condensed (or deposited) at different temperatures, whereas Schmitt et al. (2015) and Mouzay et al. (2021) compared the spectra of a sample condensed at 130 K and then cooled it down to 60 K, or 70 K, respectively. While we have compared how the temperature affects the state of crystallization as a function of deposition temperature, Schmitt et al. (2015) and Mouzay et al. (2021) studied the reversible temperature effects upon cooling-warming their crystallized C_6H_6 ice at temperatures below its condensation temperature.

The difference in the shape of the band between our experimental study and the work of Schmitt et al. (2015) in which C_6H_6 is condensed at 130 K is certainly the result of the distinct spectral resolution of the data used in both experiments: 4 cm^{-1} in our work, while 1 cm^{-1} in Schmitt et al. (2015). The bands may not be fully resolved at 4 cm^{-1} resolution and can induce spectral shape changes such as wider and weaker bands

and even some spectral shifts of the order of up to 1 cm^{-1} if the band is asymmetric or if there exists a weaker side band or a shoulder at a separation less than the spectral resolution. This can explain that our experimental spectra display only a single band at 681 cm^{-1} , and maybe only part of the shift. It can also explain the width and intensity difference of the narrow 706 cm^{-1} band in Schmitt et al. (2015) and our wider less intense ν_8 ring deformation mode. However, it is difficult to fully explain the shift of the ν_4 C–H out-of-plane bending mode at 681 cm^{-1} and its strong difference in intensity between our work and Schmitt et al. (2015). Both states of crystallization may not be exactly the same. In our experiments, we used diamond as the substrate material while Schmitt et al. (2015) used cesium iodide (CsI), which may also play a role in the crystallization. We note that, except for using a different substrate material, we have no explanation for the spectral differences observed between the results of Mouzay et al. (2021; single band of ν_4 at 679 cm^{-1}) and those of Schmitt et al. (2015; ν_4 asymmetric doublet band at 679 and 681 cm^{-1}), even if using a similar laboratory technique and the same spectral resolution of 1 cm^{-1} to obtain crystalline C_6H_6 ices and look at their temperature spectral dependence.

Compared to the Vinatier et al. (2018) C_6H_6 ice cloud emission feature at 682 cm^{-1} , our data at 130 K gives a peak frequency of the ν_4 band of crystalline C_6H_6 ice 1 cm^{-1} lower in energy.

Schmitt et al. (2015) have also provided the real and imaginary parts of the ice complex refractive index of benzene ice at 130 K from 400 to 4200 cm^{-1} available in the SSHADE⁵ database. Complex refractive indices, which are temperature dependent (as we show in Figures 8 and 9), are crucial to determine the abundances of condensed species observed in

⁵ Solid Spectroscopy Hosting Architecture of Databases and Expertise (<https://www.sshade.eu/>).

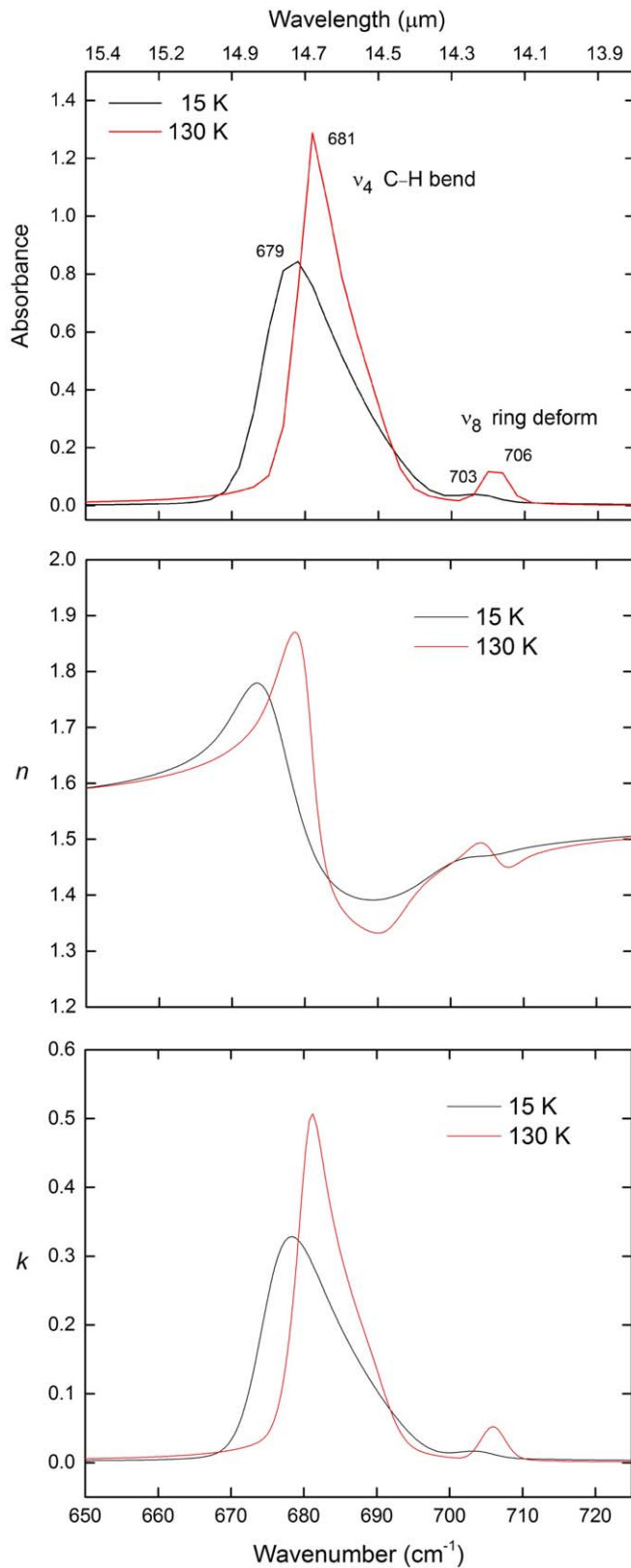


Figure 9. Absorbance spectra and associated optical constants (real part n and imaginary part k of the complex refractive index) for the ν_4 C–H asymmetric bending mode of C_6H_6 ice in the amorphous phase at 15 K (black curve) and in the crystalline phase at 130 K (red curve). C_6H_6 ice was formed by direct vapor deposition at 15 and 130 K to produce thin ice films of 3.87 and 3.63 μm , respectively, which were analyzed by FTIR spectroscopy from 50 to 8000 cm^{-1} (200–1.25 μm).

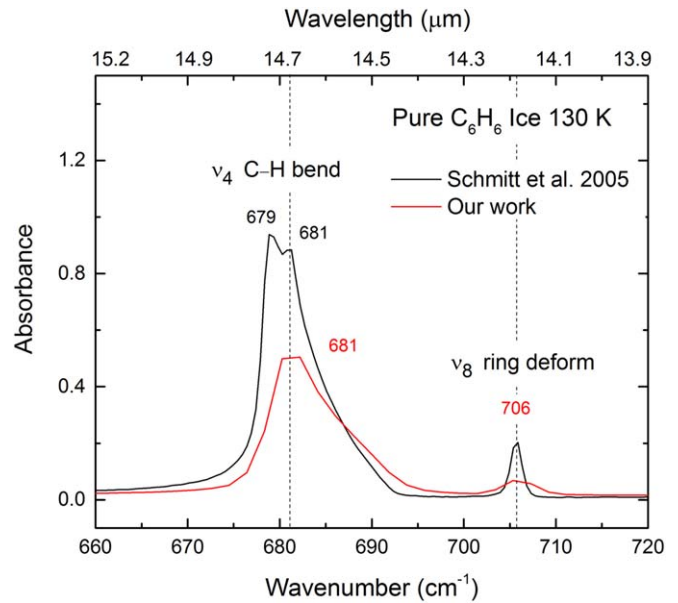


Figure 10. Comparisons of laboratory absorbance spectra of crystalline C_6H_6 ice from Schmitt et al. (2015) and our data obtained under similar experimental conditions using the SPECTRAL chamber (current work). The black curve shows the Schmitt et al. (2015) absorbance spectrum at 130 K obtained from a C_6H_6 thin ice film of 1.65 μm using a spectral resolution of 1 cm^{-1} , while the red curve depicts the absorbance spectrum from this work recorded at a spectral resolution of 4 cm^{-1} , in which C_6H_6 vapor was deposited at 130 K to form a thin ice film of 1.65 μm . Superimposed in each figure are the vibrational transitions and peak frequencies for each observed ice absorption band.

planetary atmospheres. Moreover, for low-temperature environments, such as Titan’s atmosphere and surface, where thermal energy is at a minimum, it is essential to obtain experimental optical data in the far-IR spectral region that has high thermal emission below 400 cm^{-1} , where CIRS has measured in detail during the 13 yr Cassini mission, and for which optical constants of organic ices observed in Titan’s stratosphere are still lacking. In our work, we have generated a wide database of optical constants of benzene ice from 50 cm^{-1} up to 8000 cm^{-1} in order to provide critically missing experimental spectroscopic and optical data for C_6H_6 ice needed to continue interpreting Cassini-observed spectra of Titan’s atmosphere.

Regarding the CIRS-observed HASP ice cloud detected by Anderson et al. (2018b) in Titan’s late southern fall stratosphere at high southern latitudes, its emission feature peaks near 200 cm^{-1} (see Figure 19 in Anderson et al. 2018b). The vertical extent of the HASP ice cloud is observed at stratospheric altitudes where pure C_6H_6 , pure hydrogen cyanide (HCN), and pure cyanoacetylene (HC_3N) are expected to condense and form stratospheric ice clouds (see Figure 1). In Titan’s atmosphere, most of the organic vapors will condense to form ice shells on aerosol solid particles as the vapors cool while descending throughout Titan’s stratosphere. The C_6H_6 ice spectra that we have obtained in this study did not display any detectable absorption bands between 50 and 400 cm^{-1} (100–25 μm), for any of the deposition temperatures studied (15–130 K). With our FTIR instrument and experimental protocol, we are able to detect absorption bands at this wavenumber range with an absorbance height as low as 0.002 absorbance unit (for $S/N > 3$). For example, we

detected the weak far-IR absorption bands of propionitrile between 100 and 390 cm^{-1} (see Anderson et al. 2018b; Nna-Mvondo et al. 2019). This was not the case for C_6H_6 ice. The HASP ice cloud has a very intense and broad far-IR spectral feature centered at 200 cm^{-1} (Anderson et al. 2018b). Compared with those previous measurements of other molecules absorbing in this frequency range integrated with other observed ice cloud bands that we carried out with the same experimental setup and method (Anderson et al. 2018a, 2018b; Nna-Mvondo et al. 2019), we should be able to detect such an intense and wide band around 200 cm^{-1} if it was present for C_6H_6 ice. Additionally, other published far-IR spectral studies of solid benzene (Chantry et al. 1967; Harada & Shimanouchi 1967, 1971; Sataty et al. 1973; Sataty & Ron 1976) did not detect any absorption band around 200 cm^{-1} . So we agree that we can rule out C_6H_6 ice as the only absorber of the HASP ice cloud spectral feature.

Therefore, our results definitely rule out pure C_6H_6 ice as the spectral match of the HASP cloud emission feature. However, as reported in Anderson et al. (2018b), the HASP ice cloud could be formed by a co-condensation scenario, in which Titan's organic vapors, including benzene, enter altitude regions in the stratosphere where the HASP cloud is observed and where they can simultaneously saturate to form a mixed (or co-condensed) ice cloud. In addition to the HASP ice cloud, ice cloud formation processes in Titan's stratosphere via vapor co-condensation have already been reported for the formation of the northern winter 160 cm^{-1} ice cloud observed in Titan's northern winter lower stratosphere (Anderson & Samuelson 2011; Anderson et al. 2018a). This 160 cm^{-1} ice cloud was experimentally determined to contain (at a minimum) co-condensed HCN and HC_3N .

5. Conclusion

To the best of our knowledge, our work is the first publication of far- and mid-IR absorbance spectra of benzene ice conducted over a large range of deposition temperatures. We have provided the associated optical constants for each of the studied temperatures from 15 to 130 K. These spectra and optical constants generated from cold to warmer temperatures provide valuable data for research related to Titan's stratosphere but also to Titan's surface. Indeed, solid benzene has been tentatively identified on Titan's surface (Niemann et al. 2005; Clark et al. 2010). Our low-temperature data of C_6H_6 ices (<80 K) are also useful for the investigation of other cold astronomical environments where benzene has been observed, such as in the atmospheres of Jupiter (Kim et al. 1985) and Saturn (Bézard et al. 2001), and in the protoplanetary nebula CRL 618 (Cernicharo et al. 2001).

D.N.-M. and C.M.A. acknowledge research funding support by the NASA Internal Scientist Funding Model (ISFM) through the Fundamental Laboratory Research (FLaRe) work package. D.N.-M acknowledges also internal funding support by the Center for Space Sciences and Technology (CSST) of the University of Maryland, Baltimore County (UMBC).

ORCID iDs

Delphine Nna-Mvondo  <https://orcid.org/0000-0001-7107-4988>

References

- Allamandola, L. J., Tielens, A. G. G. M., & Barker, J. R. 1989, *ApJS*, **71**, 733
- Anderson, C. M., Nna-Mvondo, D., Samuelson, R. E., McLain, J. L., & Dworkin, J. P. 2018a, *ApJ*, **865**, 62
- Anderson, C. M., & Samuelson, R. E. 2011, *Icar*, **212**, 762
- Anderson, C. M., Samuelson, R. E., Achterberg, R. K., Barnes, J. W., & Flasar, F. M. 2014, *Icar*, **243**, 129
- Anderson, C. M., Samuelson, R. E., & Nna-Mvondo, D. 2018b, *SSRv*, **214**, 125
- Andrew, E. R., & Eades, R. G. 1953, *RSPSA*, **218**, 537
- Angell, C. A., Sare, J. M., & Sare, E. J. 1978, *JPhCh*, **82**, 2622
- Bertie, J. E., & Keefe, C. D. 2004, *JMoSt*, **695**, 39
- Bézard, B., Drossart, P., Encrenaz, T., & Feuchtgruber, H. 2001, *Icar*, **154**, 492
- Bittner, J. D., & Howard, J. B. 1981, *Symp. (Int.) Combust.*, **18**, 1105
- Bonadeo, H., Marzocchi, M. P., Castellucci, E., & Califano, S. 1972, *JChPh*, **57**, 4299
- Buss, R. H., Jr., Tielens, A. G. G. M., Cohen, M., et al. 1993, *ApJ*, **415**, 250
- Callahan, M. P., Gerakines, P. A., Martin, M. G., Peeters, Z., & Hudson, R. L. 2013, *Icar*, **226**, 1201
- Cernicharo, J., Heras, A. M., Tielens, A. G. G. M., et al. 2001, *ApJL*, **546**, L123
- Chantry, G. W., Gebbie, H. A., Lassier, B., & Wyllie, G. 1967, *Natur*, **214**, 163
- Cherchneff, I. 2011, *EAS Publ. Ser.*, **46**, 177
- Clark, R. N., Curchin, J. M., Barnes, J. W., et al. 2010, *JGRE*, **115**, E10005
- Clemett, S. J., Maechling, C. R., Zare, R. N., et al. 1994, *Metic*, **29**, 457
- Coates, A. J., Crary, F. J., Lewis, G. R., et al. 2007, *GeoRL*, **34**, L22103
- Coustenis, A., Bampasidis, G., Achterberg, R. K., et al. 2013, *ApJ*, **779**, 177
- Coustenis, A., Jennings, D. E., Achterberg, R. K., et al. 2016, *Icar*, **270**, 409
- Coustenis, A., Jennings, D. E., Achterberg, R. K., et al. 2018, *ApJL*, **854**, L30
- Domingo, M., Millán, C., Satorre, M. A., & Cantó, J. 2007, *Proc. SPIE*, **6616**, 66164A
- Dubochet, J., Alba, C. M., MacFarlane, D. R., et al. 1984, *JPhCh*, **88**, 6727
- Epstein, H., & Steiner, W. 1934, *Natur*, **133**, 910
- Fray, N., & Schmitt, B. 2009, *P&SS*, **57**, 2053
- Frenklach, M., & Feigelson, E. D. 1989, *ApJ*, **341**, 372
- Hahn, J. H., Zenobi, R., Bada, J. L., & Zare, R. N. 1988, *Sci*, **239**, 1523
- Harada, I., & Shimanouchi, T. 1967, *JChPh*, **46**, 2708
- Harada, I., & Shimanouchi, T. 1971, *JChPh*, **55**, 3605
- Hayatsu, R., Matsuoka, S., Scott, R. G., Studier, M. H., & Anders, E. 1977, *GeCoA*, **41**, 1325
- Herzberg, G. 1945, *Molecular Spectra and Molecular Structure. Vol. 2: Infrared and Raman Spectra of Polyatomic Molecules* (New York, NY: Van Nostrand-Reinhold)
- Hirschfeld, T., & Mantz, A. W. 1976, *ApSpe*, **30**, 552
- Hollenberg, J. L., & Dows, D. A. 1962, *JChPh*, **37**, 1300
- Ishii, K., Nakayama, H., Yoshida, T., Usui, H., & Koyama, K. 1996, *Bull. Chem. Soc. Jpn.*, **69**, 2831
- Khanna, R. K., Ospina, M. J., & Zhao, G. 1988, *Icar*, **73**, 527
- Khare, B. N., Bakes, E. L. O., Imanaka, H., et al. 2002, *Icar*, **160**, 172
- Kim, S. J., Caldwell, J., Rivolo, A. R., Wagener, R., & Orton, G. S. 1985, *Icar*, **64**, 233
- Kim, Y. S., & Kaiser, R. I. 2009, *ApJS*, **181**, 543
- Lebonnois, S., Bakes, E. L. O., & McKay, C. P. 2002, *Icar*, **159**, 505
- Leger, A., & Puget, J. L. 1984, *A&A*, **500**, 279
- Mair, R. D., & Hornig, D. F. 1949, *JChPh*, **17**, 1236
- Materese, C. K., Nuevo, M., & Sandford, S. A. 2015, *ApJ*, **800**, 116
- Miani, A., Cané, E., Palmieri, P., Trombetti, A., & Handy, N. C. 2000, *JChPh*, **112**, 248
- Mimura, K. 1995, *GeCoA*, **59**, 579
- Mouzay, J., Couturier-Tamburelli, I., Piétri, N., & Chiavassa, T. 2021, *JGRE*, **126**, e06566
- Niemann, H. B., Atreya, S. K., Bauer, S. J., et al. 2005, *Natur*, **438**, 779
- Nna-Mvondo, D., Anderson, C. M., & Samuelson, R. E. 2019, *Icar*, **333**, 183
- Pering, K. L., & Ponnamperna, C. 1971, *Sci*, **173**, 237
- Rocha, W., & Pilling, S. 2014, *AcSpA*, **123**, 436
- Romanescu, C., Marschall, J., Kim, D., Khatiwada, A., & Kalogerakis, K. S. 2010, *Icar*, **205**, 695
- Sagan, C., Khare, B. N., Thompson, W. R., et al. 1993, *ApJ*, **414**, 399
- Sataty, Y. A., & Ron, A. 1976, *JChPh*, **65**, 1578
- Sataty, Y. A., Ron, A., & Brith, M. 1973, *CPL*, **23**, 500
- Schinder, P. J., Flasar, F. M., Marouf, E. A., et al. 2011, *Icar*, **215**, 460
- Schmitt, B., Vinatier, S., & Bernard, J. M. 2015, *Mid-IR Transmission and Optical Constants Spectra of Crystalline C₆H₆ at 130 K. SSHADE/GhoSST (OSUG Data Center). Dataset/Spectral Data*
- Shock, E. L., & Schulte, M. D. 1990, *Natur*, **343**, 728

- Simoneit, B. R. T., & Fetzner, J. C. 1996, *OrGeo*, 24, 1065
- Teanby, N. A., Sylvestre, M., Sharkey, J., et al. 2019, *GeoRL*, 46, 3079
- Tempelmeyer, K. E., & Mills, D. W., Jr. 1968, *JAP*, 39, 2968
- Tielens, A. G. G. M. 2013, in *Planets, Stars and Stellar Systems: Vol. 5*, ed. T. D. Oswalt & G. Gilmore (Dordrecht: Springer), 499
- Tielens, A. G. G. M., & Charnley, S. B. 1997, in *Planetary and Interstellar Processes Relevant to the Origins of Life*, ed. D. C. B. Whittet (Dordrecht: Springer), 23
- Trainer, M. G., Pavlov, A. A., Jimenez, J. L., et al. 2004, *GeoRL*, 31, L17S08
- Vinatier, S., Schmitt, B., Bézard, B., et al. 2018, *Icar*, 310, 89
- Vuitton, V., Yelle, R. V., & Cui, J. 2008, *JGRE*, 113, E05007
- Waite, J. H., Young, D. T., Cravens, T. E., et al. 2007, *Sci*, 316, 870
- Wang, H., & Frenklach, M. 1997, *CoFI*, 110, 173
- Wilson, E. B., Jr. 1934, *PhRv*, 45, 706
- Wilson, E. B., Decius, J. C., & Cross, P. C. 1955, *Molecular Vibrations: The Theory of Infrared and Raman Vibrational Spectra* (New York: McGraw-Hill)
- Wilson, E. H., Atreya, S. K., & Coustenis, A. 2003, *JGRE*, 108, 5014
- Wyatt, R. E. 1998, *JChPh*, 109, 10732
- Zhou, L., Kaiser, R. I., & Tokunaga, A. T. 2009, *P&SS*, 57, 830